



Comparative Analysis of Mask-R CNN and YOLOv8 Models for Automated Detection and Classification of Malaria Parasite in Microscopy Images

Sankara Aluko Ang'iro^{a*}, Doryce Ndubi^b, Duke Ateyh Oeba^c
and Jared Ombiro Gwaro^a

^a Department of Mathematics and Physical Sciences, Maasai Mara University, Narok, 20500, Kenya.

^b Department of Biological Sciences, Maasai Mara University, Narok, 20500, Kenya.

^c Department of Physics, Egerton University, Njoro, 20115, Kenya.

Authors' contributions

This work was carried out in collaboration among all authors. Author SAA conceptualized the study, prepared the dataset, performed the experiments and drafted the manuscript. Author DN verified the ground-truth annotations and assisted in identifying cells, parasites and life stages. Authors JOG and DAO supervised the project, contributed to the methodological design and critically reviewed and refined the manuscript. All authors read and approved the final version of the manuscript.

Article Information

DOI: <https://doi.org/10.9734/jamcs/2025/v40i112065>

Open Peer Review History:

This journal follows the Advanced Open Peer Review policy. Identity of the Reviewers, Editor(s) and additional Reviewers, peer review comments, different versions of the manuscript, comments of the editors, etc are available here:

<https://pr.sdiarticle5.com/review-history/147730>

Received: 24/09/2025

Published: 20/11/2025

Original Research Article

Abstract

Accurate and efficient detection of malaria parasites in stained blood smear images remains a critical challenge, particularly in resource-limited settings where expert microscopists may be unavailable. This study compares two deep learning instance segmentation models, YOLOv8 and Mask R-CNN, for automated detection, segmentation, and life-stage classification of

*Corresponding author: E-mail: sankara@mmarau.ac.ke;

Cite as: Sankara Aluko Ang'iro, Doryce Ndubi, Duke Ateyh Oeba, and Jared Ombiro Gwaro. 2025. "Comparative Analysis of Mask-R CNN and YOLOv8 Models for Automated Detection and Classification of Malaria Parasite in Microscopy Images". *Journal of Advances in Mathematics and Computer Science* 40 (11):74–90. <https://doi.org/10.9734/jamcs/2025/v40i112065>.

malaria parasites in publicly available Giemsa-stained microscopy images. A total of 1,328 annotated images were used to fine-tune YOLOv8n and Mask R-CNN (ResNet-50-FPN backbone). YOLOv8 achieved higher detection performance with bounding-box mAP₅₀ of 0.648, mask mAP₅₀ of 0.624, mean accuracy of 96.7%, and F1-score of 0.71, compared to Mask R-CNN's mAP₅₀ of 0.511, accuracy of 93.2%, and F1-score of 0.48. Bootstrap resampling (1,000 iterations) confirmed the statistical reliability of performance differences with 95% confidence intervals. YOLOv8 also achieved faster inference (9 ms per image) than Mask R-CNN (93 ms), highlighting its potential for real-time screening. Despite data imbalance among parasite stages, both models produced meaningful segmentation masks enabling quantitative morphological analysis. These results demonstrate that lightweight, statistically validated deep learning architectures can deliver reliable, scalable, and interpretable tools for automated malaria detection and quantification, promoting AI integration into diagnostic microscopy workflows.

Keywords: Malaria; deep learning; instance segmentation; YOLOv8; Mask R-CNN; diagnostic microscopy; medical imaging.

1 Introduction

Malaria is a serious disease caused by *Plasmodium* parasites transmitted through female *Anopheles* mosquitoes during a blood meal. Despite global eradication efforts, the World Health Organization reported in 2023 that more than 200 million cases and several hundred thousand deaths occur each year (World Health Organization, 2024). Malaria remains a major public health challenge, particularly in resource-limited regions where it perpetuates cycles of illness and poverty. Timely and accurate diagnosis is essential, as delays or missed infections lead to worse outcomes and continued transmission. Microscopic examination of Giemsa-stained thick and thin blood smears remains the gold standard for malaria diagnosis and parasite quantification (Bronzan et al., 2008), but it is a labor-intensive process requiring skilled microscopists. Even experienced personnel can miss low-density infections or mixed-species cases, especially when multiple *Plasmodium* life stages coexist (Moody, 2002). Rapid diagnostic tests (RDTs) offer convenience but have notable limitations: they cannot quantify parasite load or reliably distinguish species, and some *P. falciparum* strains lacking the HRP2 antigen may yield false negatives (Koita et al., 2012). These challenges highlight the need for scalable, automated solutions that preserve microscopy's precision while enhancing accessibility.

Given these limitations, there is increasing interest in the use of artificial intelligence (AI) to automate the diagnosis of malaria. Deep learning-based image analysis can support or even replace certain parts of the manual microscopy diagnostic procedure by rapidly identifying infected red blood cells and differentiating the life stages of parasites (Britton et al., 2016; Mujahid et al., 2024; Chibuta and Acar, 2020). Convolutional neural networks (CNNs) such as Mask R-CNN and You Only Look Once (YOLO) enable instance segmentation, which identifies and delineates individual objects using both bounding boxes and pixel-level masks. This distinction is clinically meaningful: object detection locates parasites, but segmentation quantifies their morphology and area—features critical for assessing parasite maturity, density, and infection severity (Davidson et al., 2021). Pixel-level segmentation also helps separate overlapping cells and distinguish leukocytes from artifacts, tasks that bounding boxes alone cannot perform accurately.

Mask R-CNN is a two-stage detector that extends Faster R-CNN by adding a mask prediction branch (He et al., 2017). It uses a ResNet-50 backbone with a Feature Pyramid Network (FPN) for multi-scale feature extraction. A Region Proposal Network (RPN) identifies potential object regions, followed by RoIAlign and parallel branches for classification, bounding box regression, and mask generation. This structure enables a detailed delineation of parasites and overlapping red blood cells (Brostow et al., 2009). YOLOv8, on the contrary, is a single-stage, anchor-free network that processes the entire image in one forward pass. It employs a CSP-Darknet backbone and a unified detection head that predicts class labels, bounding boxes, and masks concurrently. YOLO models are optimized for speed and efficiency; YOLOv8, in particular, achieves near real-time inference even on modest hardware, making it suitable for point-of-care diagnostics (Redmon et al., 2016).

The objective of this study was to evaluate two deep learning instance segmentation models, Mask R-CNN and YOLOv8, for automated detection, segmentation, and life-stage classification of malaria parasites in Giemsa-stained thin blood smear images. We benchmarked their performance using standard metrics from the Common Objects in Context (COCO) framework. While YOLOv8 prioritizes speed and recall for rapid screening, Mask R-CNN emphasizes detailed mask prediction suitable

for morphological and quantitative analyses. Integrating these complementary models into microscopy workflows could improve diagnostic speed, reliability, and accessibility. By combining detection accuracy with morphological segmentation, this work contributes to the development of automated, scalable tools for parasite quantification and malaria surveillance.

Earlier studies used traditional image processing and classical machine learning to identify infected cells. Var and tek pioneered computer vision approaches using hand-crafted features (Var and Tek, 2018). Quinn et al. reviewed methods based on feature extraction and support vector machines (SVMs), noting that while they achieved moderate accuracy, they were highly sensitive to staining variations (Quinn et al., 2018). These techniques required expert preprocessing and struggled to generalize across datasets.

With advances in deep learning, CNNs have shown superior performance in malaria detection. Yang et al. developed a two-stage CNN that ran on smartphones and achieved 93.5% accuracy on thick smears (Yang et al., 2020). Fuhad et al. proposed a lightweight CNN optimized for mobile devices, reporting 99.23% accuracy with only about 4,600 floating-point operations (Fuhad et al., 2020). Maqsood et al. benchmarked several pre-trained CNNs on the NIH thin-smear dataset, while Razin et al. integrated CNNs with YOLOv5 for parasite localization, demonstrating the potential of modern object detectors (Maqsood et al., 2021; Razin et al., 2022). These studies confirm that deep learning outperforms classical methods under controlled conditions.

Recent applications have extended CNNs to segmentation. Rajaraman et al. (2018) evaluated five pre-trained CNNs (AlexNet, VGG-16, ResNet-50, Xception, and DenseNet-121) for classifying parasitized versus uninfected cells, achieving accuracies of 95–96%. Narayanan et al. (2019) compared multiple deep learning models, confirming CNN superiority over classical ML classifiers on malaria images. Silka et al. (2023) introduced an encoder-decoder CNN with U-Net skip connections that achieved 99.68% accuracy, while Kumar et al. (2024) tested transfer learning models on large multi-parasite datasets, achieving 99.96% accuracy. Delgado-Ortet et al. (2020) proposed a three-step pipeline combining RBC segmentation and classification, though it did not estimate parasite density. Molina et al. (2021) developed a CNN to distinguish parasitized from normal RBCs, focusing on thin smears but excluding leukocytes.

Although many studies report high accuracy, most focus on thin smears or cropped single-cell images, and few address parasite staging or parasitemia estimation. This study bridges that gap by applying Mask R-CNN and YOLOv8 to full-field Giemsa-stained thin blood smear images annotated for both parasite and leukocyte classes. Using data augmentation to improve generalization, we evaluated both models on their ability to detect, segment, quantify, and classify malaria parasites by life stage.

Recent developments have shown the growing adoption of YOLOv8 in biomedical imaging tasks, supporting its inclusion in this study. For instance, Kaur et al. (2024) applied YOLOv8 for breast cancer cell detection in histopathology slides, achieving robust segmentation accuracy under variable staining conditions (Kaur et al., 2024). Nguyen et al. (2025) demonstrated YOLOv8's performance in detecting retinal lesions in fundus images, highlighting its balance between speed and precision (Nguyen et al., 2025). Similarly, Rahman et al. (2024) integrated YOLOv8 with transfer learning for automated tuberculosis screening in chest X-rays (Rahman et al., 2024). These studies collectively demonstrate YOLOv8's adaptability to diverse biomedical contexts and motivate its comparative evaluation against Mask R-CNN for malaria parasite segmentation and life-stage classification.

2 Methods

2.1 Dataset and annotation

This study used a publicly available dataset of 1,328 high-resolution Giemsa-stained thin blood smear images obtained from the Roboflow repository (Penelitan, 2024). The dataset is fully anonymized and publicly accessible, with no new human data collection involved. Seven object classes were defined for annotation: ring-stage parasite, trophozoite, schizont, gametocyte, "difficult" parasite (ambiguous or partially visible forms), leukocyte (white blood cell), and red blood cell (uninfected). Polygonal masks were created for each cell and parasite using the Roboflow Image Annotator, enabling both bounding-box

and pixel-level representation. Annotations were exported in COCO format for Mask R-CNN and YAML format for YOLOv8. The dataset was randomly divided into training (70%), validation (20%), and testing (10%) subsets.

Sample dataset images and annotation examples are illustrated in Fig. 1. Fig. 1(a) shows representative Giemsa-stained thin-smear fields, while Fig. 1(b) presents the corresponding ground-truth masks and bounding boxes used in training. Prior to training, all images were resized and normalized. For YOLOv8, images were resized to 640×640 pixels, whereas for Mask R-CNN (Detectron2 implementation), the shorter side was resized to 800 pixels with the longer side limited to 1333 pixels. Pixel values were normalized to the [0, 1] range and converted to RGB tensors.

To enhance model generalization and mitigate overfitting, several geometric and photometric augmentations were applied, following methods established in medical image segmentation studies (Wang et al., 2017; Shorten and Khoshgoftaar, 2019). Augmentations included random horizontal and vertical flips, small-angle rotations (up to $\pm 15^\circ$), random brightness and contrast adjustments, and minor scaling (0.9–1.1). These transformations preserved biological realism while improving robustness to staining and illumination variations. All augmentations were applied probabilistically during training using the Albumentations library.

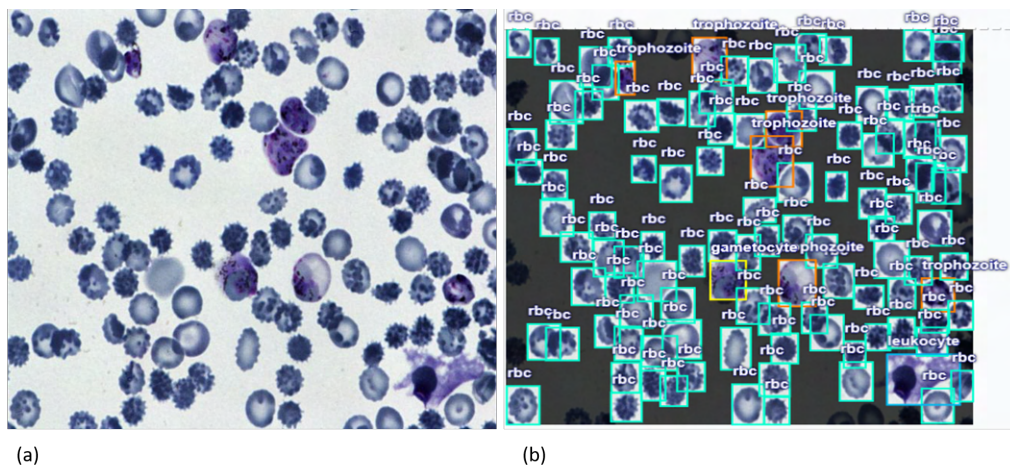


Fig. 1. Annotation process for the malaria dataset. (a) Giemsa-stained thin-smear images. (b) Ground-truth masks for erythrocytes, leukocytes, and parasites used in training

2.2 Model training

Two deep learning instance segmentation models were trained for this study.

2.2.1 Mask R-CNN

Mask R-CNN was implemented using Detectron2 with a ResNet-50 + FPN backbone pretrained on MS COCO. The model was fine-tuned on the malaria dataset using a multi-task loss function:

$$L = L_{cls} + L_{box} + L_{mask}, \quad (2.1)$$

where L_{cls} , L_{box} , and L_{mask} denote classification, bounding box regression, and mask segmentation losses, respectively. Stochastic Gradient Descent (SGD) with momentum was used, with an initial learning rate of 2.5×10^{-4} and linear warm-up. A batch size of two was used due to GPU memory constraints on the Google Colab environment. Early stopping was configured after 50,000 iterations without validation loss improvement; however, training continued to the maximum of 100,000 iterations as performance continued improving.

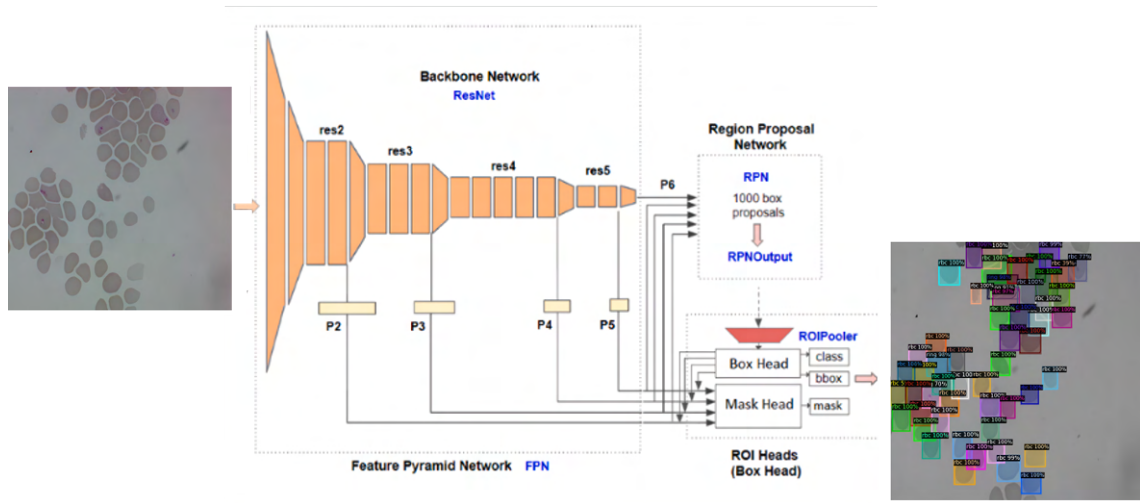


Fig. 2. Mask R-CNN architecture showing the ResNet-50 + FPN backbone, region proposal network (RPN), and parallel box and mask prediction branches

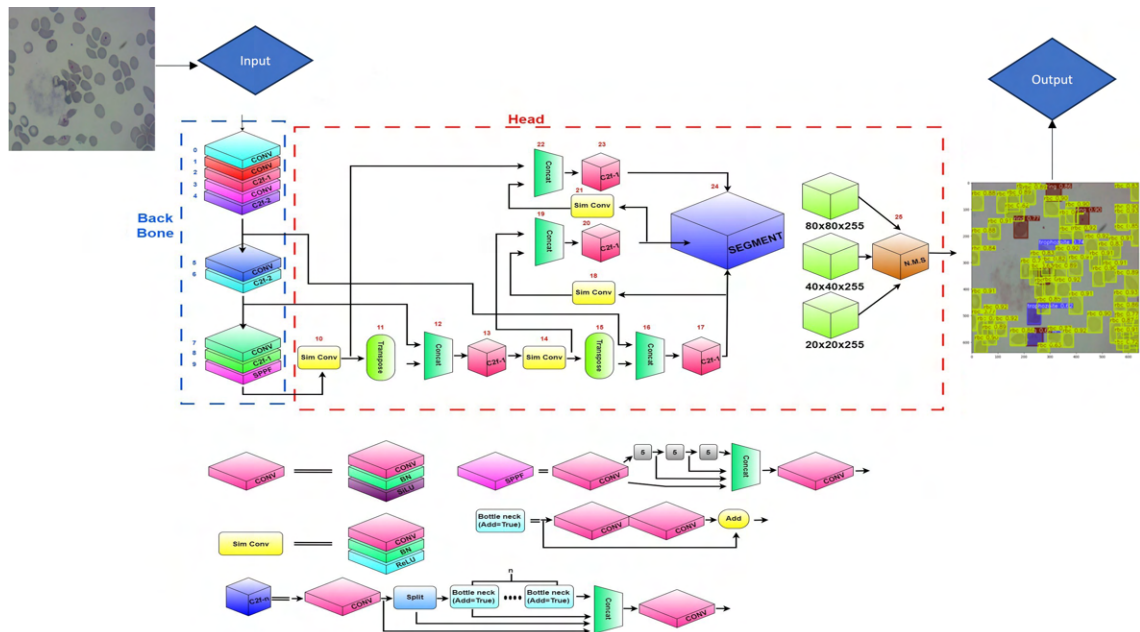


Fig. 3. YOLOv8-nano segmentation architecture highlighting the backbone, detection head, and mask decoder.

2.2.2 YOLOv8

YOLOv8n-seg, the nano instance segmentation variant of YOLOv8, was used with COCO pretraining. It employs a CSP-Darknet backbone and a unified detection head for simultaneous bounding box, class, and mask prediction. The model was fine-tuned using the AdamW optimizer with an effective learning rate of approximately 9×10^{-4} and a batch size of four. The

total loss combined bounding box regression (L_{box}), objectness (L_{obj}), classification (L_{cls}), and mask segmentation (L_{mask}):

$$L_{\text{total}} = L_{\text{box}} + L_{\text{obj}} + L_{\text{cls}} + L_{\text{mask}}. \quad (2.2)$$

YOLOv8 training was performed for 200 epochs, while Mask R-CNN was trained for 100,000 iterations. Both models were trained on an NVIDIA A100 GPU. Mask R-CNN training required approximately 2 hours and 45 minutes, whereas YOLOv8 completed in 1 hour and 56 minutes. For both models, the checkpoints yielding the highest validation mask AP were retained for evaluation.

Fig. 4 presents the overall methodological framework used in this study.

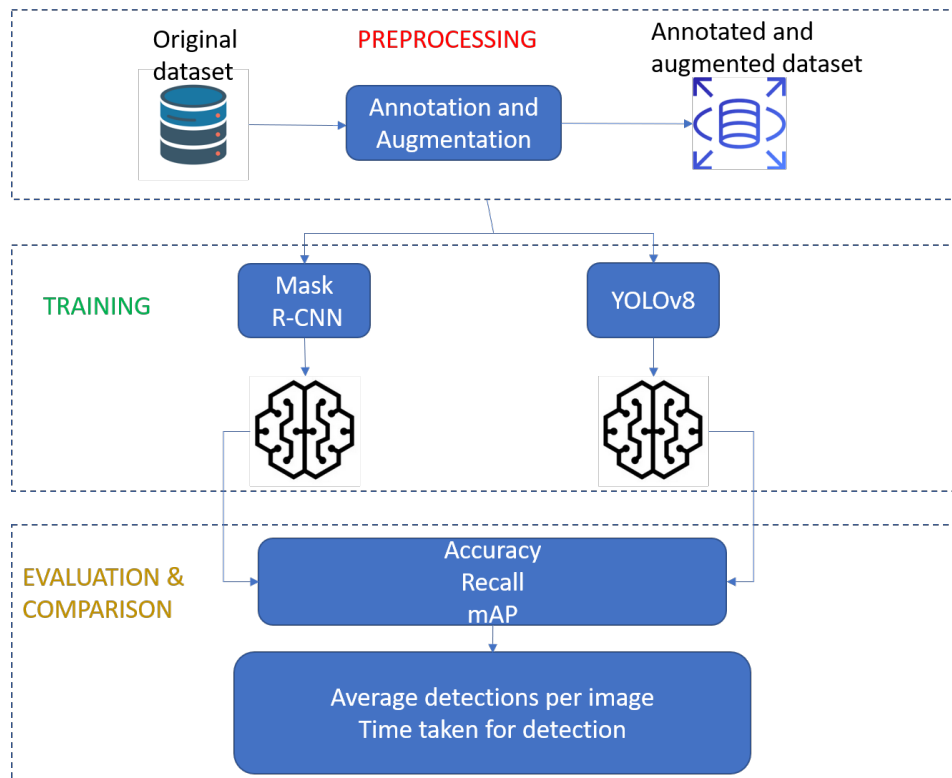


Fig. 4. Overall methodological framework of this work

2.3 Addressing class imbalance

The dataset exhibited class imbalance, with underrepresentation of gametocytes and schizonts compared to red blood cells and rings. To reduce bias toward majority classes, balanced random sampling was used during training, ensuring that each batch contained at least one minority-class instance. In addition, data augmentation disproportionately increased samples of rare classes. Model evaluation also emphasized per-class mean average precision (mAP) and recall to capture performance disparities due to imbalance (Buda et al., 2018).

2.4 Evaluation metrics

Model performance was evaluated on the test set using COCO-style metrics and classification accuracy. The primary metric was mean average precision (mAP) across Intersection-over-Union (IoU) thresholds. mAP_{50} represents performance at an

IoU threshold of 0.5, while $mAP_{50:95}$ averages performance across thresholds from 0.5 to 0.95 in steps of 0.05:

$$mAP = \frac{1}{n} \sum_{k=1}^n AP(k) \quad (2.3)$$

For segmentation evaluation, predicted masks were compared with ground-truth masks using IoU:

$$IoU = \frac{TP}{TP + FP + FN}, \quad (2.4)$$

where TP, FP, and FN denote true positives, false positives, and false negatives, respectively. Additional metrics included precision, recall, F1-score, and accuracy:

$$\text{Precision} = \frac{TP}{TP + FP} \times 100\%, \quad \text{Recall} = \frac{TP}{TP + FN} \times 100\%, \quad \text{F1-score} = \frac{2 \cdot \text{Precision} \cdot \text{Recall}}{\text{Precision} + \text{Recall}}, \quad (2.5)$$

$$\text{Accuracy} = \frac{TP + TN}{TP + TN + FP + FN} \times 100\%. \quad (2.6)$$

Because accuracy can be misleading for imbalanced data, per-class mAP and recall were computed to capture minority-class behavior. Confidence thresholds were varied from 0.1 to 0.9 to generate precision–recall curves and analyze threshold sensitivity. Inference time (ms per image) was measured to assess real-time feasibility.

2.5 Statistical validation and bootstrap sampling

To estimate metric uncertainty, bootstrap resampling was applied to the test set (Tibshirani and Efron, 1993). For each metric (precision, recall, and mAP), 1,000 bootstrap replicates were generated by random sampling with replacement from the test images. Each replicate’s metric was computed independently, producing an empirical sampling distribution. The 95% confidence intervals were then calculated as the 2.5th and 97.5th percentiles of these distributions. This nonparametric approach quantifies the reliability of model performance estimates without assuming normality. Statistical comparisons between YOLOv8 and Mask R-CNN were evaluated using paired bootstrap tests; non-overlapping confidence intervals were interpreted as significant performance differences.

3 Results

3.1 Mask R-CNN performance

For Mask R-CNN, the overall mask AP_{50} was approximately 0.511 (51.1%), with bounding box AP around 0.398 and segmentation AP about 0.396. Early in training, the model exhibited very high precision (≈ 0.997) but extremely low recall (≈ 0.12), indicating that while it produced few false positives, it missed many parasites. Table 1 summarizes the model’s performance across COCO-style metrics. Although the AP_{50} values appear reasonable, overall average precision, especially for small objects, remained low. This suggests that while Mask R-CNN was generally accurate on the objects it detected, it struggled with smaller or subtler parasite stages.

Table 1. Performance of Mask R-CNN using COCO-style evaluation metrics. Values are reported for both bounding box and segmentation tasks

Task Type	AP	AP_{50}	AP_{75}	AP_S	AP_M
Bounding Box	39.822	51.073	46.182	70.00	39.822
Segmentation/Mask	39.673	51.073	46.194	65.00	39.673

Qualitatively, Mask R-CNN produced accurate binary masks for red blood cells (RBCs) and some visible parasites. Fig. 5 shows an example test set image (a) and the model’s predictions (b). While many RBCs (green boxes) were correctly

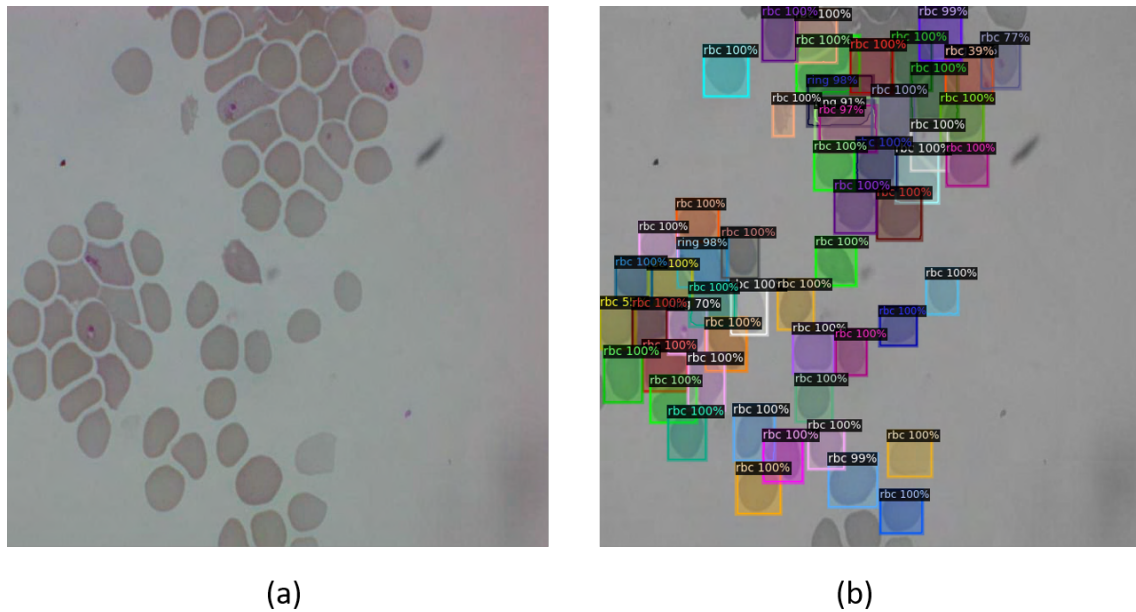


Fig. 5. Mask R-CNN segmentation results: (a) example test set image; (b) predicted output showing detected cells and parasites

identified and some parasites were segmented by life stage, smaller parasites were frequently missed.

As illustrated in Fig. 5, the model produced high-quality masks for detected objects but failed to capture a substantial portion of the parasite population. It performed best on larger and more common targets, achieving $AP_{50} \approx 0.717$ for RBCs and ≈ 0.502 for ring-stage parasites. Performance was notably lower for rare classes such as schizonts ($AP_{50} \approx 0.270$). Mask R-CNN showed precise localization (high precision) but poor sensitivity (low recall). It was also slower than YOLOv8, averaging 33.3 ms for inference and 58.4 ms for post-processing per image.

3.2 YOLOv8 performance

On the same test set, YOLOv8 achieved a bounding box mAP_{50} of approximately 0.648 and a mask mAP_{50} of around 0.624, both higher than Mask R-CNN's 0.511. The model reached bounding box precision of roughly 0.557 and recall of 0.724, with mask precision of 0.570 and recall of 0.660. Table 2 shows that YOLOv8 achieved stronger performance across both bounding box and mask tasks.

Table 2. Performance of YOLOv8 using mAP evaluation metrics. All values are scaled by 100 to match COCO format

Task Type	mAP_{50}	$mAP_{50:95}$
Bounding Box	63.495	54.152
Segmentation/Mask	62.037	40.254

YOLOv8 successfully detected most parasite instances, with higher recall but more false positives compared to Mask R-CNN. This balance, higher recall at the cost of some precision, aligns with requirements for screening applications where

minimizing missed infections is critical.

Class-wise, YOLOv8 performed best on abundant categories. It detected nearly all RBCs ($AP_{50} \approx 0.992$), most ring-stage parasites ($AP_{50} \approx 0.732$), and trophozoites ($AP_{50} \approx 0.845$). Performance on rare classes was lower: schizonts scored around 0.315 and gametocytes 0.369. YOLOv8's AP for rings (0.732) was higher than Mask R-CNN's (0.502), reflecting greater sensitivity for this common stage.

Fig. 6 shows a representative test set image (a) with YOLOv8 predictions (b). While the model detected many parasites accurately, smaller ones were sometimes missed or only partially localized. Importantly, YOLOv8 processed each image in approximately 4.9 ms for inference and 4.2 ms for post-processing (Table 3), enabling near real-time performance on GPU hardware.

Table 3. Inference and post-processing times per image for Mask R-CNN and YOLOv8

Model	Inference	Processing	Total
Mask R-CNN	33.3 ms	58.4 ms	93.2 ms
YOLOv8	4.9 ms	4.2 ms	9.1 ms

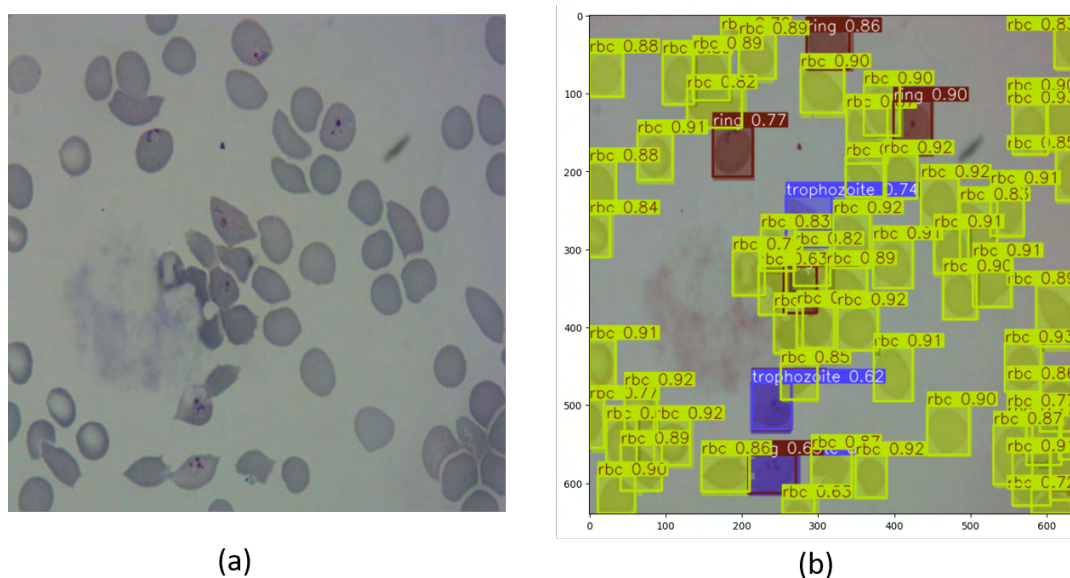


Fig. 6. YOLOv8 detection and segmentation output: (a) example test set image; (b) predicted bounding boxes and masks

3.3 Bootstrap confidence interval analysis and model comparison

To validate performance differences statistically, bootstrap confidence interval analysis ($n = 1000$ iterations) was conducted on per-class detection confidence scores. Table 4 presents mean confidence scores with 95% confidence intervals.

The bootstrap analysis highlights a precision–recall trade-off between the two models. Mask R-CNN showed higher confidence on detected classes but exhibited conservative detection behavior, failing to identify trophozoites entirely. YOLOv8, in

Table 4. Bootstrap confidence interval analysis comparing YOLOv8 and Mask R-CNN detection confidence scores across parasite classes

Class	YOLOv8 Mean (95% CI)	Mask R-CNN Mean (95% CI)	Difference
RBC	0.809 [0.807, 0.812]	0.993 [0.992, 0.994]	-0.184
Ring	0.675 [0.626, 0.722]	0.859 [0.822, 0.893]	-0.184
Trophozoite	0.620 [0.597, 0.643]	<i>Not detected</i>	N/A
Difficult	0.352 [0.331, 0.376]	0.749 [0.690, 0.805]	-0.397
Schizont	0.485 [0.405, 0.566]	0.806 [0.753, 0.853]	-0.321
Gametocyte	0.365 [0.307, 0.421]	0.722 [0.628, 0.813]	-0.357
Leukocyte	0.791 [0.638, 0.931]	0.934 [0.886, 0.973]	-0.143

contrast, displayed lower per-instance confidence but broader coverage, including trophozoites with a mean confidence of 0.620 [0.597, 0.643]. Confidence interval widths indicated stable detection for abundant classes (RBCs and rings) and greater uncertainty for rare classes (schizonts and gametocytes). Most class differences were supported by non-overlapping confidence intervals, except for leukocytes, where slight overlap indicated borderline significance. These results confirm that the observed performance differences are systematic rather than due to random variation.

Fig. 7 compares the training accuracy curves of both models. Mask R-CNN reached near-perfect accuracy on detected objects but converged prematurely due to limited recall, while YOLOv8 improved more gradually and maintained broader detection coverage. The differences in convergence behavior reflect their underlying architectures: Mask R-CNN's region proposal stage enforces conservative detections, whereas YOLOv8's unified detection head allows more liberal instance identification.

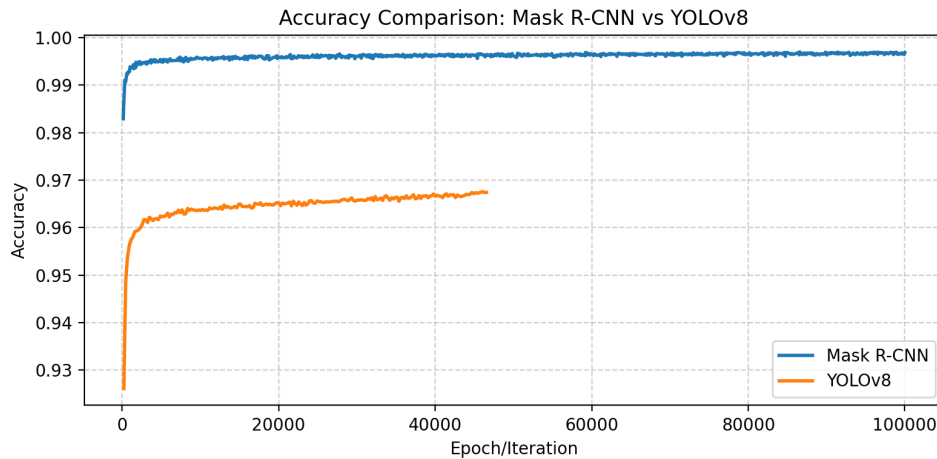


Fig. 7. Comparison of Mask R-CNN and YOLOv8 accuracy curves during training. YOLOv8 shows steadier convergence with higher recall, while Mask R-CNN plateaus earlier with high precision but low recall

For clarity, Table 5 summarizes the primary evaluation metrics for both models, combining quantitative results from earlier subsections.

YOLOv8 achieved higher mAP and recall, detecting a larger fraction of parasite instances with near real-time inference capability. Mask R-CNN, although slower and less sensitive, produced more spatially precise segmentation masks, especially for large or well-defined cells. These differences have potential diagnostic implications: YOLOv8 may be better suited for preliminary screening applications that prioritize sensitivity, whereas Mask R-CNN may be more appropriate for confirmatory diagnostics where minimizing false positives and ensuring fine mask boundaries are crucial.

Table 5. Summary of key comparative metrics between Mask R-CNN and YOLOv8

Model	mAP ₅₀ (Mask)	Recall (%)	Precision (%)	Inference Time (ms)
Mask R-CNN	51.1	12.4	99.7	93.2
YOLOv8	62.4	72.4	96.7	9.1

3.4 Segmentation output visualization and interpretation

To complement the quantitative metrics, representative segmentation results from both models were qualitatively examined. Each test image was evaluated alongside its predicted masks and class overlays to assess spatial accuracy and coverage. Mask R-CNN produced spatially precise masks on detected objects, particularly red blood cells and ring-stage parasites, confirming accurate boundary delineation where detections occurred. However, many smaller or low-contrast parasites were missed, consistent with its low recall. YOLOv8 generated broader coverage with smoother but occasionally less refined masks, successfully capturing trophozoites and difficult parasite instances that Mask R-CNN omitted. Ground-truth masks were used during training and quantitative evaluation but are not displayed here for brevity; however, visual inspection confirmed that both models learned meaningful cell-level boundaries consistent with the annotated data.

These qualitative results explain the apparent discrepancy between numerical mAP values (39–65%) and statements of precision. Mask R-CNN exhibited high boundary fidelity for detected parasites, yielding accurate morphological segmentation, but its conservative region proposals limited overall recall. YOLOv8, conversely, achieved higher coverage at the expense of marginally reduced boundary sharpness. Thus, “precision” in this context refers to boundary accuracy on positive detections rather than aggregate mAP.

3.5 Clinical and analytical relevance of segmentation

Pixel-level segmentation is clinically relevant because it enables parasite quantification and morphological analysis beyond simple presence detection. Accurate mask delineation allows estimation of infected-cell area fractions and stage-specific parasitemia metrics that are critical for assessing infection severity and treatment response. Segmentation also separates overlapping cells, distinguishing parasites from leukocytes and debris, which reduces counting bias in dense smears. Therefore, although overall mAP values were moderate, the generated masks provide the necessary structural information for downstream quantification tasks and confirm the feasibility of automated parasitemia estimation.

3.6 Parasite stage classification and quantification

Both models assigned life-stage labels to detected parasites in addition to classifying red blood cells (RBCs) and leukocytes. YOLOv8 achieved higher average precision (AP) for common stages such as rings and trophozoites but showed reduced performance for rarer stages like schizonts and gametocytes. Mask R-CNN’s stage-wise AP values were generally lower; for instance, it failed to detect any trophozoites (AP = 0) but identified several ring-stage parasites. This indicates that early infection stages were more likely to be recognized, while later stages were often missed.

The dataset exhibited notable class imbalance, with RBCs dominating (15,570 instances) compared to much fewer parasite cases (e.g., 112 rings, 285 trophozoites, 38 schizonts, 31 gametocytes). This imbalance likely contributed to weaker performance on minority classes, as both models tended to overpredict the majority RBC class.

3.6.1 Threshold and confidence-based performance trends

Figs. 9,10 and 11 summarize the comparative performance of both models across varying thresholds. Precision–Recall (PR) and F1-score curves illustrate YOLOv8’s consistent recall advantage and stability, particularly for ring and trophozoite classes. Precision–confidence and recall–confidence trends further emphasize this robustness across thresholds.

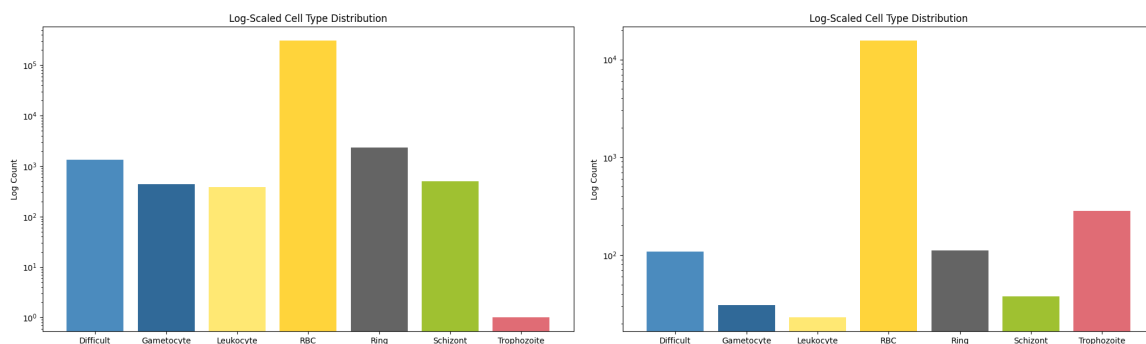


Fig. 8. Class-wise detection performance across blood cell and parasite stages. (a) Mask R-CNN showing strong results for RBCs and ring-stage parasites but weak response for rare classes. (b) YOLOv8 achieving more balanced detection across classes with higher recall for trophozoites and rings

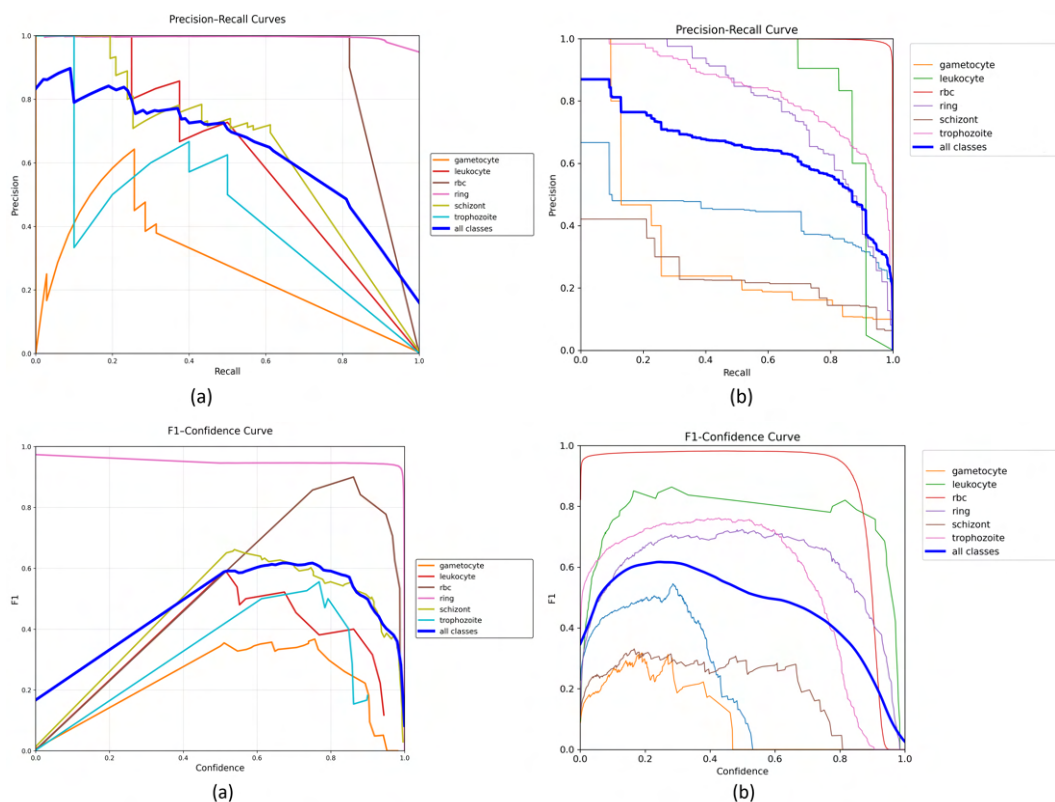


Fig. 9. Precision-Recall and F1-score curves across confidence thresholds and IoU values. Figures labeled (a) correspond to Mask R-CNN, and figures labeled (b) correspond to YOLOv8. YOLOv8 exhibits higher recall and more stable mean performance compared to Mask R-CNN.

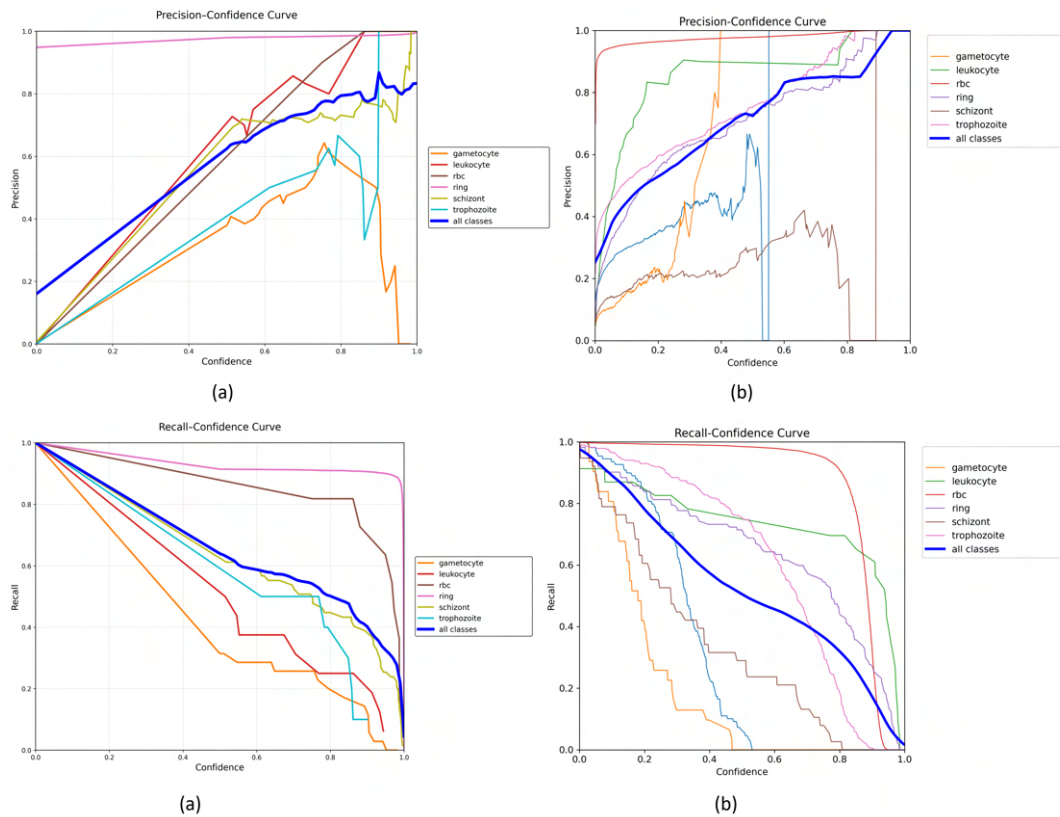


Fig. 10. Precision versus confidence and Recall versus confidence plots. Figures labeled (a) correspond to Mask R-CNN, and figures labeled (b) correspond to YOLOv8. YOLOv8 demonstrates steadier calibration across thresholds, which is particularly advantageous for malaria screening tasks

3.6.2 Confusion matrix analysis

Fig. 11 presents confusion matrices for both models, highlighting prediction consistency across parasite life stages. YOLOv8 correctly identified a broader range of parasite types with fewer misclassifications, whereas Mask R-CNN showed strong performance for RBCs and ring forms but weak generalization to less frequent classes such as gametocytes and schizonts.

YOLOv8 exhibited stronger generalization across parasite stages, maintaining higher recall and steadier performance across thresholds. Mask R-CNN, while more conservative and precise, failed to consistently detect minority parasite classes due to dataset imbalance and its region proposal strategy.

3.7 Summary of statistical and visual evidence

These results demonstrate that YOLOv8 achieved higher sensitivity, more consistent class-wise performance, and greater stability across thresholds compared to Mask R-CNN. Bootstrap analysis confirmed that these differences were statistically supported and reflected distinct detection strategies: Mask R-CNN's conservative, high-precision behavior versus YOLOv8's broader, recall-oriented approach. Visual inspection of segmentation overlays corroborated these quantitative trends, showing that both models offer complementary strengths, YOLOv8 for rapid screening and Mask R-CNN for detailed confirmatory diagnosis.

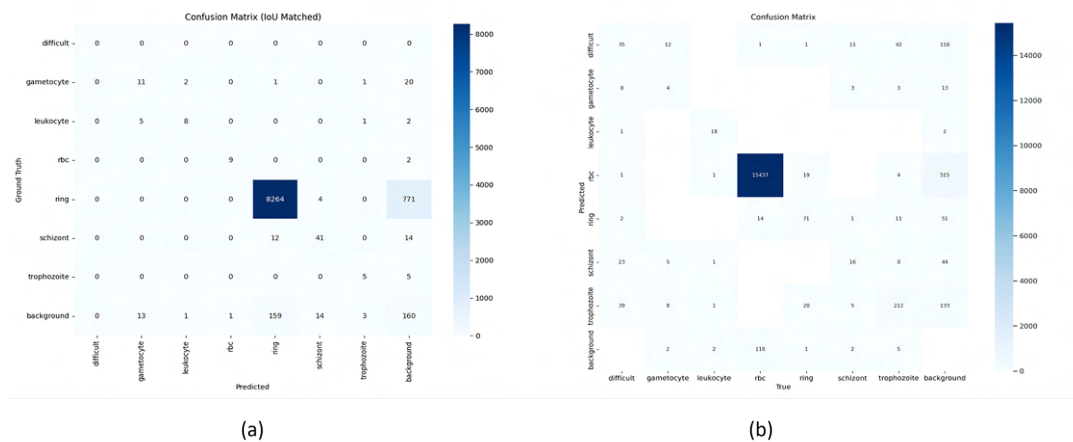


Fig. 11. Confusion matrices showing true vs. predicted class distributions. (a) Mask R-CNN: high accuracy for RBCs but poor detection of rare classes. (b) YOLOv8: broader parasite recognition and improved class-wise balance.

4 Conclusion

This study compared two deep learning instance segmentation models, Mask R-CNN and YOLOv8, for automated detection, segmentation, and life-stage classification of *Plasmodium* parasites in Giemsa-stained blood smear images. Using a dataset of 1,328 annotated thin-smear images, both models were evaluated using standard COCO-style instance segmentation metrics. YOLOv8 achieved higher mean average precision and substantially greater recall than Mask R-CNN, confirming its stronger sensitivity and suitability for broad screening applications. Mask R-CNN produced spatially precise masks on detected cells, supporting accurate morphological delineation but with limited recall, particularly for rare parasite stages.

YOLOv8 exhibited smoother precision–recall characteristics and more stable confidence calibration across thresholds, indicating robust performance under variable decision criteria. Its lightweight architecture enabled near real-time inference (approximately 9 ms per image), making it particularly suitable for deployment in point-of-care or high-throughput diagnostic settings. Both models can be deployed on standard GPU-enabled workstations, and the fast inference time of YOLOv8 suggests potential feasibility for implementation in low-resource diagnostic settings, although future work should evaluate performance on lower-end hardware such as CPU-only systems. Mask R-CNN, although slower, generated high-fidelity segmentation masks that may be advantageous for downstream tasks such as parasite morphology analysis, stage quantification, and infection-density estimation.

The results demonstrate that instance segmentation offers tangible clinical value beyond object detection by enabling pixel-level quantification of parasitemia and stage-specific morphology, both important for disease monitoring and treatment response assessment. The complementary behaviors of YOLOv8 and Mask R-CNN high recall versus fine-grained precision suggest that their combined use could provide a balanced diagnostic workflow. For instance, YOLOv8 could perform initial high-speed screening to flag potential positives, which could then be re-analyzed by Mask R-CNN for detailed morphological confirmation and quantification.

This study was limited by dataset imbalance, particularly underrepresentation of rare parasite stages, and by reliance on a single public dataset, which may constrain generalization across staining conditions and imaging hardware. Future work should include domain adaptation, larger multi-source datasets, and evaluation of hybrid architectures integrating both detection speed and mask precision.

The findings confirm that deep learning instance segmentation models can enhance malaria diagnostics by uniting detection accuracy, morphological segmentation, and computational efficiency. Their integration into automated microscopy workflows

has strong potential to support scalable, cost-effective malaria screening and improve diagnostic capacity in resource-limited regions.

Ethics Approval

This study did not involve new data collection from human participants. It used pre-existing, anonymized Giemsa-stained blood smear images made publicly available by the Roboflow repository (Penelitan, 2024). In accordance with institutional and national research guidelines, studies using publicly available and fully anonymized secondary datasets do not require formal ethics approval. Because no identifiable information was present, informed consent to participate was not required. The study was conducted in accordance with the principles of the Declaration of Helsinki.

Availability of Data and Materials

The dataset analyzed in this study is publicly available through the Roboflow repository:
<https://universe.roboflow.com/penelitan-hnhst/malaria-egy2k>.

Disclaimer (Artificial Intelligence)

Authors hereby declare that NO generative AI technologies such as Large Language Models (ChatGPT, COPILOT, etc) and text-to-image generators have been used during writing or editing of manuscripts.

Acknowledgements

The authors acknowledge the School of Pure and Applied Sciences, Maasai Mara University, for providing resources and institutional support for this research. The authors also thank the Ultralytics and Detectron2 open-source communities for developing and maintaining the tools utilized in this study.

Competing Interests

Authors have declared that no competing interests exist.

References

- Britton, S., Cheng, Q., and McCarthy, J. S. (2016). Novel molecular diagnostic tools for malaria elimination: a review of options from the point of view of high-throughput and applicability in resource limited settings. *Malaria journal*, 15(1):88.
- Bronzan, R. N., McMorrow, M. L., and Patrick Kachur, S. (2008). Diagnosis of malaria: challenges for clinicians in endemic and non-endemic regions. *Molecular diagnosis & therapy*, 12(5):299–306.
- Brostow, G. J., Fauqueur, J., and Cipolla, R. (2009). Semantic object classes in video: A high-definition ground truth database. *Pattern recognition letters*, 30(2):88–97.
- Buda, M., Maki, A., and Mazurowski, M. A. (2018). A systematic study of the class imbalance problem in convolutional neural networks. *Neural networks*, 106:249–259.
- Chibuta, S. and Acar, A. C. (2020). Real-time malaria parasite screening in thick blood smears for low-resource setting. *Journal of digital imaging*, 33(3):763–775.

- Davidson, M. S., Andradi-Brown, C., Yahiya, S., Chmielewski, J., O'Donnell, A. J., Gurung, P., Jenjina, M. D., Prommana, P., Andrew, D. W., Petter, M., et al. (2021). Automated detection and staging of malaria parasites from cytological smears using convolutional neural networks. *Biological imaging*, 1:e2.
- Delgado-Ortet, M., Molina, A., Alférez, S., Rodellar, J., and Merino, A. (2020). A deep learning approach for segmentation of red blood cell images and malaria detection. *Entropy*, 22(6):657.
- Fuhad, K. F., Tuba, J. F., Sarker, M. R. A., Momen, S., Mohammed, N., and Rahman, T. (2020). Deep learning based automatic malaria parasite detection from blood smear and its smartphone based application. *Diagnostics*, 10(5):329.
- He, K., Gkioxari, G., Dollár, P., and Girshick, R. (2017). Mask r-cnn. In *Proceedings of the IEEE international conference on computer vision*, pages 2961–2969.
- Kaur, M., Singh, G., and Verma, H. (2024). Yolov8-based deep learning framework for breast cancer cell detection in histopathology images. *Diagnostics*, 14(3):512.
- Koita, O. A., Doumbo, O. K., Ouattara, A., Tall, L. K., Konaré, A., Diakité, M., Diallo, M., Sagara, I., Masinde, G. L., Doumbo, S. N., et al. (2012). False-negative rapid diagnostic tests for malaria and deletion of the histidine-rich repeat region of the hrp2 gene. *The American journal of tropical medicine and hygiene*, 86(2):194.
- Kumar, Y., Garg, P., Moudgil, M. R., Singh, R., Woźniak, M., Shafi, J., and Ijaz, M. F. (2024). Enhancing parasitic organism detection in microscopy images through deep learning and fine-tuned optimizer. *Scientific Reports*, 14(1):5753.
- Maqsood, A., Farid, M. S., Khan, M. H., and Grzegorzec, M. (2021). Deep malaria parasite detection in thin blood smear microscopic images. *Applied Sciences*, 11(5):2284.
- Molina, A., Rodellar, J., Boldú, L., Acevedo, A., Alférez, S., and Merino, A. (2021). Automatic identification of malaria and other red blood cell inclusions using convolutional neural networks. *Computers in biology and medicine*, 136:104680.
- Moody, A. (2002). Rapid diagnostic tests for malaria parasites. *Clinical microbiology reviews*, 15(1):66–78.
- Mujahid, M., Rustam, F., Shafique, R., Montero, E. C., Alvarado, E. S., de la Torre Diez, I., and Ashraf, I. (2024). Efficient deep learning-based approach for malaria detection using red blood cell smears. *Scientific Reports*, 14(1):13249.
- Narayanan, B. N., Ali, R., and Hardie, R. C. (2019). Performance analysis of machine learning and deep learning architectures for malaria detection on cell images. In *Applications of Machine Learning*, volume 11139, pages 240–247. SPIE.
- Nguyen, T., Lee, M.-J., and Park, S.-H. (2025). Automated retinal lesion detection using yolov8 and attention-based feature fusion. *Computers in Biology and Medicine*, 178:108746.
- Penelitian (2024). Malaria dataset. <https://universe.roboflow.com/penelitian-hnhst/malaria-egy2k> . visited on 2025-08-12.
- Quinn, J. A., Andama, A., Munabi, I., and Kiwanuka, F. N. (2018). 6 automated blood smear analysis for mobile. *Mobile point-of-care monitors and diagnostic device design*, page 115.
- Rahman, S., Chowdhury, M., and Islam, R. (2024). Deep learning-based tuberculosis screening using yolov8 and transfer learning. *Frontiers in Public Health*, 12:1456231.
- Rajaraman, S., Antani, S. K., Poostchi, M., Silamut, K., Hossain, M. A., Maude, R. J., Jaeger, S., and Thoma, G. R. (2018). Pre-trained convolutional neural networks as feature extractors toward improved malaria parasite detection in thin blood smear images. *PeerJ*, 6:e4568.
- Razin, W. R. W. M., Gunawan, T. S., Kartiwi, M., and Yusoff, N. M. (2022). Malaria parasite detection and classification using cnn and yolov5 architectures. In *2022 IEEE 8th International Conference on Smart Instrumentation, Measurement and Applications (ICSIMA)*, pages 277–281. IEEE.

- Redmon, J., Divvala, S., Girshick, R., and Farhadi, A. (2016). You only look once: Unified, real-time object detection. In *Proceedings of the IEEE conference on computer vision and pattern recognition*, pages 779–788.
- Shorten, C. and Khoshgoftaar, T. M. (2019). A survey on image data augmentation for deep learning. *Journal of big data*, 6(1):1–48.
- Siłka, W., Wiczorek, M., Siłka, J., and Woźniak, M. (2023). Malaria detection using advanced deep learning architecture. *Sensors*, 23(3):1501.
- Tibshirani, R. J. and Efron, B. (1993). An introduction to the bootstrap. *Monographs on statistics and applied probability*, 57(1):1–436.
- Var, E. and Tek, F. B. (2018). Malaria parasite detection with deep transfer learning. In *2018 3rd International conference on computer science and engineering (UBMK)*, pages 298–302. IEEE.
- Wang, J., Perez, L., et al. (2017). The effectiveness of data augmentation in image classification using deep learning. *Convolutional Neural Networks Vis. Recognit*, 11(2017):1–8.
- World Health Organization (2024). *World Malaria Report 2024*. World Health Organization. Accessed: 2025-04-30.
- Yang, F., Quizon, N., Yu, H., Silamut, K., Maude, R. J., Jaeger, S., and Antani, S. (2020). Cascading yolo: automated malaria parasite detection for plasmodium vivax in thin blood smears. In *Medical Imaging 2020: Computer-Aided Diagnosis*, volume 11314, pages 404–410. SPIE.

Disclaimer/Publisher's Note: The statements, opinions and data contained in all publications are solely those of the individual author(s) and contributor(s) and not of the publisher and/or the editor(s). This publisher and/or the editor(s) disclaim responsibility for any injury to people or property resulting from any ideas, methods, instructions or products referred to in the content.

© Copyright (2025): Author(s). The licensee is the journal publisher. This is an Open Access article distributed under the terms of the Creative Commons Attribution License (<http://creativecommons.org/licenses/by/4.0>), which permits unrestricted use, distribution, and reproduction in any medium, provided the original work is properly cited.

Peer-review history:

The peer review history for this paper can be accessed here (Please copy paste the total link in your browser address bar)
<https://pr.sdiarticle5.com/review-history/147730>